New Journal of Physics
The open-access journal for physics

Atomic structure of the ultrathin alumina on NiAl(110) and its antiphase domain boundaries as seen by frequency modulation dynamic force microscopy

G H Simon, T König, H-P Rust, M Heyde[1] and H-J Freund
Fritz-Haber-Institut der Max-Planck-Gesellschaft, Faradayweg 4-6,
D-14195 Berlin, Germany
E-mail: heyde@fhi-berlin.mpg.de

New Journal of Physics **11** (2009) 093009 (16pp)
Received 27 April 2009
Published 14 September 2009
Online at http://www.njp.org/
doi:10.1088/1367-2630/11/9/093009

Abstract. Atomically resolved frequency modulation dynamic force microscopy (FM-DFM) images of the ultrathin alumina film on NiAl(110) are presented. Images show in detail the surface unit cell, both types of antiphase domain boundaries (translation-related domain boundaries) and lateral displacements within these types of boundaries. Due to the loss of translational symmetry at the boundary, structures of even increased complexity are revealed. Lateral models for these local arrangements have been created on the basis of adjusted unit cell structures. FM-DFM produces on this surface a contrast of extraordinarily high surface sensitivity. It matches the topmost oxygen layer even with respect to topographic height, which adds the third dimension to the analysis. With this the antiphase domain boundaries are shown to be shallow depressions. Furthermore, new symmetry aspects have been found in the topography of these boundaries. The local structure of the film surface shows evidence of substrate influence in its topography and the domain boundary network shows indications that its growth behaviour is affected by this interaction in its very details beyond sheer appearance. Presented results can be linked to the relation between growth and structure of an emerging class of structurally related ultrathin alumina films.

[1] Author to whom any correspondence should be addressed.

Contents

1. Introduction

Recent frequency modulation dynamic force microscopy (FM-DFM) results from the ultrathin alumina film on NiAl(110) exhibited a contrast of extraordinarily high surface sensitivity [1]. Atomic resolution images accurately reproduced the topography of the surface and its highly complex unit cell. This surface sensitivity is not commonly available in e.g. scanning tunneling microscopy (STM) at equal lateral resolution and provides additional or complementary information to STM. It makes FM-DFM well suited to study even more complex surface structures namely the atomic details of the film's characteristic antiphase domain boundary (APDB) network. Domain boundaries within reconstructed surfaces or thin films have frequently made their appearance in the literature [2]–[7]. As striking topographic features breaking the translational symmetry of the surface, they do naturally attract attention. They are intimately linked to the mechanisms governing the growth of one material onto another like lattice mismatches, chemical bonds and surface phase transitions [8]. Means to study them are, for example, spot profile analysis of low energy electron diffraction (SPA-LEED) [9] and scanning probe microscopies including FM-DFM and STM. However, the subject has so far not been the focus of atomic resolution force microscopy studies. There are only a few cases given in the literature [10]–[14] and even therein the imaged boundaries are sometimes not considered in the analysis in detail. Also topography is usually neglected and attention is paid soley to lateral arrangements at the boundary. Here we give an example of an oxidic surface and present for the first time atomically resolved FM-DFM images of domains and APDBs in the ultrathin crystalline alumina on NiAl(110). Structural features are presented that have not been described in the literature before. The film surface shows a specific network of line defects—few reflection domain boundaries and many of what SPA-LEED has shown to be APDBs [15]. These boundaries separate domains of the same reflection orientation. Questions related to line defects, i.e. domain boundaries, in this particular surface are, besides their obviously rich structure, to do with the availability of special adsorption sites and the permeability towards metallic adsorbates. These questions arose during deposition studies with transition metals and molecules in the field of model catalysis [16]. In this context, STM has also been used to describe the line defect network of these domain boundaries in the film and high-resolution images have been obtained [15, 17, 18]. However, it turned out that interpretation of those STM data suffered from the difficulty to assign images with different contrasts to individual atomic layers of the film. In the analysis of (oxide) thin films, this problem frequently occurs in STM

studies and also involves mixed contributions from film and substrate due to the close proximity of the interface [19, 20]. Eventually, only substantial input from density functional theory (DFT) calculations produced a reliable model of the unit cell structure and that of one APDB [21, 22]. The film shows a remarkably large and complex surface unit cell with a variety of sites at close proximity. Upon extension at the domain boundaries, this cell gains further different sites as can be seen from the images presented in the following. Here we focus exclusively on both types of antiphase domain boundaries within one reflection domain.

2. Experimental

All data have been recorded for samples in ultrahigh vacuum (UHV) at cryogenic temperature (5 K). The microscope in use is a custom built dual-mode FM-DFM/STM [23] situated in a helium bath cryostat. It is equipped with a quartz tuning fork sensor which comprises a cut Pt/Ir wire attached with insulating epoxy adhesive to one quartz prong as a tip. Current is detected through a 50 μm wire soldered to the tip. This separates the tunneling current from force sensing via the tuning fork electrodes [24, 25]. For FM-DFM, the microscope is operated in the frequency modulation mode at a small constant oscillation amplitude $A_{\mathrm{OSC}} = 3.8$ Å. Frequency shift is used to control the tip–sample distance. All the presented images are therefore constant frequency shift topographies. In all measurements the contact potential difference has been reasonably compensated. Sensor parameters are the unperturbed resonance frequency $f_0 = 21$ kHz, spring constant $k \approx 22\,000\,\mathrm{N\,m^{-1}}$ and quality factor $Q \approx 25\,000$ of the tuning fork. A nanosurf easy PLL[2] has been used as a sensor controller together with a Nanonis system for signal processing and data acquisition.[3] The small amount of postproduction performed on the images consisted of a global levelling, adjustment of the greyscale range, cropping of images and the extraction of line profiles [26]. Due to slight thermal drift the unit cells had to be straightened out. For this the unit cell of the model [21] has been taken as a reference. Corrections were smaller than 100 pm per unit cell. This is considered negligible for images recorded over 20 min. The effect on proportions of the model's deviation from the LEED experimentally determined unit cell size is considered small. Such drift correction has been done to every image before comparison with the model and further analysis. Film preparation has been done in the usual way [27, 28].

3. Results and discussion

During this FM-DFM study, we obtained atomically resolved images from the complex surface structure of the alumina film on NiAl(110). Such high-resolution images have been recorded for both types of its APDBs within one reflection domain including previously unresolved local variations within these boundaries.

3.1. Geometry of the thin alumina film system on NiAl(110)

A schematic overview over the geometric relations between the NiAl(110) substrate and both oxide reflection domains is given in figure 1(a). The ultrathin alumina overlayer on NiAl(110) surfaces grows well ordered and two dimensional with a thickness of only 5 Å [15, 21, 27, 28]. It

[2] Nanosurf AG, Grammetstrasse 14, CH-4410 Liestal, Switzerland.
[3] SPECS Zurich GmbH, Technoparkstrasse 1, CH-8005 Zurich, Switzerland.

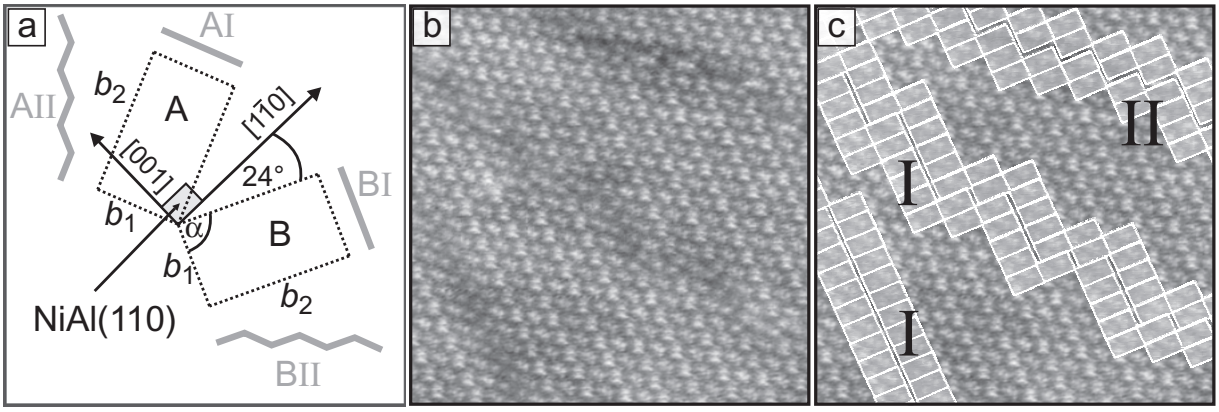

Figure 1. APDBs in a B domain of the ultrathin alumina on NiAl(110). (a) Scheme showing the geometric relation among the two oxide reflection domain unit cells, the orientation of the APDBs towards them as well as the relative orientation of the small NiAl(110) substrate unit cell. Measures of the unit cells as determined by LEED are $b_1 = 10.55$ Å, $b_2 = 17.88$ Å, $\alpha = 88.7°$ for the oxide and 2.89 Å × 4.08 Å for the substrate. In the DFT model, to which our images have been scaled to, measures are $b_1 = 10.93$ Å, $b_2 = 17.9$ Å and $\alpha = 88.16°$. The nomenclature for the domain boundaries follows [28]. The film grows incommensurate along [001] and commensurate along [1$\bar{1}$0] (matching with Ni rows of the substrate). (b) and (c): FM-DFM overview image of three APDBs visible as trenches; $\Delta f = -3.0$ Hz, $V_S = 1$ mV, $A_{OSC} = 3.8$ Å, scan area 22 nm × 22 nm. Boundaries are highlighted in the reproduction of figure 1(b) in figure 1(c) by coverage with unit cell lattices. The two left strands represent straight type I boundaries (BI) with lateral displacements appearing as steps in the APDBs whereas the top-right strand is a zigzagged type II boundary (BII).

is composed of two Al–O double layers which are oxygen terminated towards the vacuum and aluminium anchored to the substrate. Each oxide cell has the lattice constants $b_1 = 10.55$ Å, $b_2 = 17.88$ Å and their directions enclose an angle $\alpha = 88.7°$ [27]. The rectangular NiAl(110) substrate cell is 2.89 Å × 4.08 Å. Lattice vectors $\vec{b}_2$ of both reflection domains (A,B) are tilted off NiAl[1$\bar{1}$0] by ±24°. The oxide film is commensurate along NiAl[1$\bar{1}$0] and incommensurate along [001]. In the DFT model, a slightly broader unit cell is assumed to gain a commensurate unit cell of $b_1 = 10.93$ Å, $b_2 = 17.9$ Å and $\alpha = 88.16°$ [21]. The overall orientations of both types of APDBs for each reflection domain are also schematically depicted. These are the straight or type I and the zigzagged type II APDBs. Type I boundaries run parallel to the b_1 lattice direction of the respective oxide reflection domain whereas the global direction of type II boundaries follows the long diagonal of the respective unit cell. Nomenclature for the APDBs is in line with [28]. Note that the boundaries are generally thought to interrupt the film perpendicular to the substrate surface from bottom to top which actually makes them planar defects despite the minute film thickness. However, adopting the scanning probe microscopy point of view we refer to them as line defects.

APDBs are translation-related domain boundaries which occur when equivalent sites in neighbouring surface structure domains are related by a displacement vector that cannot be expressed in integer multiples of the surface structure's lattice constants. In a recent low-energy

electron microscopy study, it has been shown that such APDBs are integrated into already crystallized islands of a high-temperature grown alumina film on NiAl(110) [29]. This contradicts the hypothesis of impinging islands and corroborates the suspected relation of APDBs in the row matched film to strain relief with respect to the substrate. Early SPA-LEED studies revealed extensions of the unit cell along the NiAl[1$\bar{1}$0] direction by (3.6 ± 0.3) Å for both APDBs. This compares well, within experimental error, with the 3 Å measured by STM as the actual Burgers vectors are at angles to NiAl[1$\bar{1}$0] [15, 28]. Still the Burgers vector has a large component along the [1$\bar{1}$0] direction of the substrate which should be most efficient for strain relief in contrast to the [001] direction along which the film grows incommensurate. For the two different types of APDB, the displacement at the boundary shows different directions [28]. For the straight type I APDB, the Burgers vector is solely along the b_2 lattice direction of the oxide while type II has a component along b_1 as well as b_2. The unit cell extension has the same magnitude (3 Å) for both types of APDB. Frames (b) and (c) of figure 1 show an overview scan of a terrace covered with a B domain of the alumina film. Pairs of protrusions are visible that form rows and change orientation on adjacent rows. They enable the assignment of unit cells and subsequent correction of drift-related distortions. Furthermore, as they change orientation within the unit cell, they are not a sign for a double tip but rather indicate the oxygen-related contrast found in [1]. Stepped trenches in figure 1(b) are APDBs. They are seen best when looked at under grazing angles and along lattice axes. Positioning unit cell lattices onto the domains as depicted in figure 1(c) underlines the conclusion that the two line defects in the lower left part of the image are of type I while the one on the upper right is a type II APDB. Observed deviations from the average axis through the unit cells for both types of boundaries lead to some variety within the structure and enable the observed morphological flexibility of the APDBs. This varying appearance on the larger scale is contrasted by specific atomic arrangements involving central structural building blocks, which will become clear in this publication. For brevity, the results are presented solely for domain B but hold for the reflection domain A as well. Please note that a different assignment of domains A and B has been used in our earlier work [1].

An atomically resolved image of the unit cell of a B domain is shown in figure 2. The observed contrast gives the topography resulting from the structure of the terminating oxygen layer. It should be noted though, that the assumption that force microscopy would give the topography on any sample is too naive and not true in general. Examples have been given where contrast inversion has been observed [30]–[32]. Contrast formation is thought to depend on the short-range chemical interaction between the tip apex and the different species located at the surface directly underneath. The image is reproduced in figure 2(b) and covered for direct comparison with the theoretical model's lateral positions for the topmost oxygen (red circles) layer and the aluminium (small blue circles) layer which is lying slightly deeper. One finds a good match between theory and experiment for the oxygen sites. Aluminium positions do not appear as protrusions which also become obvious from the different numbers of sites in the model: 28 surface oxygen sites (O_S) and 24 surface aluminium sites (Al_S). Rectangular blocks of eight oxygen sites constitute important structural elements and are highlighted with green rectangles. They are present in two different orientations within the unit cell and form rows along the b_1 direction of the oxide. On these rows, blocks are connected by two diagonally opposing corners to the respective next block in the row thereby forming square groups of oxygen sites between them. The rows contain the brightest protrusions in the images and shall therefore be referred to as 'crests' in comparison to the lower lying sites forming 'troughs' between them. In figure 2(c) line profiles over such blocks of eight O sites are presented which

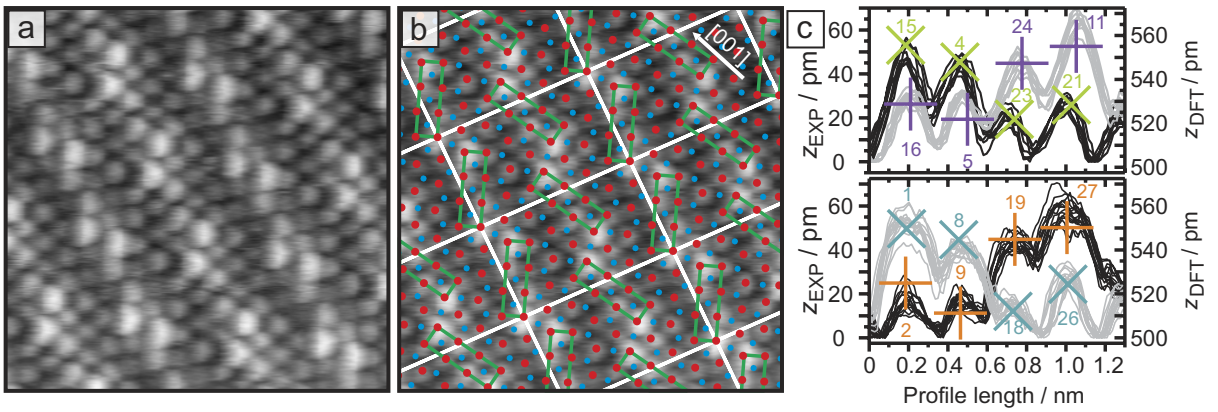

Figure 2. Atomic resolution FM-DFM image of a B domain of alumina/NiAl(110). The image is reproduced in (b) and covered with Al_S and O_S positions from the DFT model for direct comparison [21]. Green rectangles indicate the prominent structural building blocks of eight oxygen sites with their characteristic topography. Scan area 4.2 nm × 4.2 nm. $\Delta f = -2.75$ Hz, $A_{OSC} = 3.8$ Å, $V_S = -220$ mV. The diagram in (c) shows line profiles across each row of four within the two inequivalent blocks of eight oxygen sites. The crosses give the height and position along a row of four according to DFT [21] and are aligned with the respective first maximum on the left. Profiles and positions in the upper diagram correspond to the block almost aligned with NiAl[001]. The bottom diagram refers to the block of eight at a larger angle to NiAl[001]. The substrate axis is indicated by an arrow in the top right corner of (b).

highlight the topographic sensitivity of the experiment. The diagram shows 8–15 profiles for each row of four sites in such a block and for both possible orientations of this structural element (z_{EXP}). Calculated heights and lateral distances from the DFT model (coloured crosses, z_{DFT}) are given for direct comparison. The upper diagram shows the block nearly aligned with the [001] direction of the NiAl substrate, while the lower diagram shows the block which is at a larger angle to that direction. Numbers beside the crosses denote the line among the topmost oxygen sites within the coordinate table in the supplement to [21]. Note that experimentally (z_{EXP} in figure 2(c)) only relative movements of the tip are recorded and no absolute height values in the z-direction, while the model (z_{DFT}) gives absolute height with respect to a reference point above the topmost substrate nickel layer. Hence, height spans within blocks as well as relative heights of different blocks have to be compared to calculated data. Agreement between experiment and theory is better than expected. We found that the blocks almost aligned with NiAl[001] differ from the second type in their deviation from the expected glide-mirror symmetry. They lie higher, exhibit a smaller span in topographic height and they are longer. The difference in length amounts to 24 pm in the DFT model and has been determined to be 10–30 pm from several images. Once more this expresses the influence of the substrate on the film.

3.2. Straight (type I) antiphase domain boundaries

An atomically resolved FM-DFM image of a straight APDB (type B I) is shown in figure 3. Clearly visible, the boundary is marked by a fairly wide linear depression along the oxide's

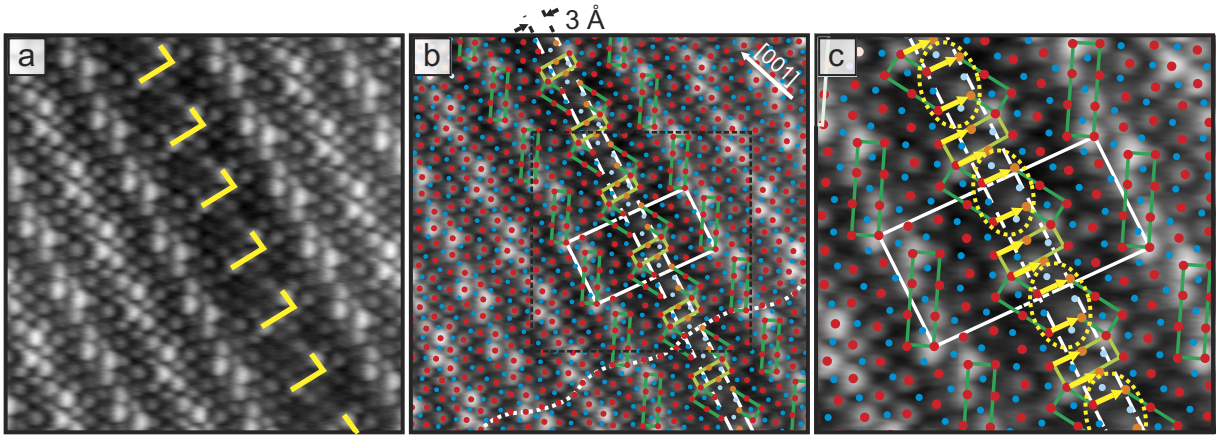

Figure 3. Atomic resolution FM-DFM image of a straight APDB (type I) in the ultrathin alumina/NiAl(110). An adjusted model [22] has been superimposed in (b). The unit cell is extended by 3 Å along b_2. Inserted sites are given in lighter colours. Dashed lines indicate the extension. The white dotted line highlights wave-like oxygen rows along the unit cell. (c) shows an enlarged section of the image for better visibility. Yellow arrows denote the direction and length (3 Å) of the Burgers vector. Yellow loops indicate spacious arrangements of oxygen sites that are different from all domain sites. Scan area 6.4 nm × 6.4 nm. The cutout measures 3.5 nm × 3.5 nm. $\Delta f = -2.75$ Hz, $A_{\mathrm{OSC}} = 3.8$ Å, $V_S = -220$ mV.

b_1-direction. The adjusted model for the lateral positions at the APDB [22] is superimposed in figure 3(b) and found to be in good agreement. This model is based on a unit cell that has been split up in the middle according to STM images. Again, the important structural elements are highlighted as well as the extended unit cell and two equivalent lines between which the inserted new sites are visible. Inserted sites shall be marked in a slightly different colour throughout this publication to distinguish them from the usual sites in the oxide unit cell: orange and light blue as compared to red and blue. In figure 3(c) an enlarged section of the elongated unit cell at the APDB is given. The atomic structure is characterized by bridge-like linear chains of oxygen sites which cross the APDB at about 10° to the b_2 lattice vector of the oxide. In the middle of the APDB a broken block of eight O atoms appears, which is of the kind that is almost aligned with the NiAl[001] direction. A particularly spacious arrangement of oxygen atoms in the shape of a quadrangle (yellow dotted loops) is formed at the boundary. This is in reasonable agreement with DFT calculations. Another deviation from the usual oxide unit cell is a rectangle of six oxygen sites which is derived from the bridging square groups indicated in light green in figure 3(c). These characterizing protrusions in the topography of the boundary form the shape of the letter 'L' as indicated by the yellow angle in figure 3(b). The Burgers vector measures 3 Å in length and is parallel to the b_2 oxide lattice vector as indicated by yellow arrows. At the same time, the Burgers vector is also parallel to the overall direction of the wavelike rows of atoms within the surface aluminium and oxygen sublattices (white dotted line in figure 3(b)). Considering the topographic quality of the contrast the domain boundary can finally be determined to be a depression. This is summarized in figure 4. An average over 167 line profiles across the APDB I covering the width of two unit cells (as indicated by the rectangle in figure 4(a)) is shown in figure 4(b). In figure 4(c), individual line profiles are shown that have

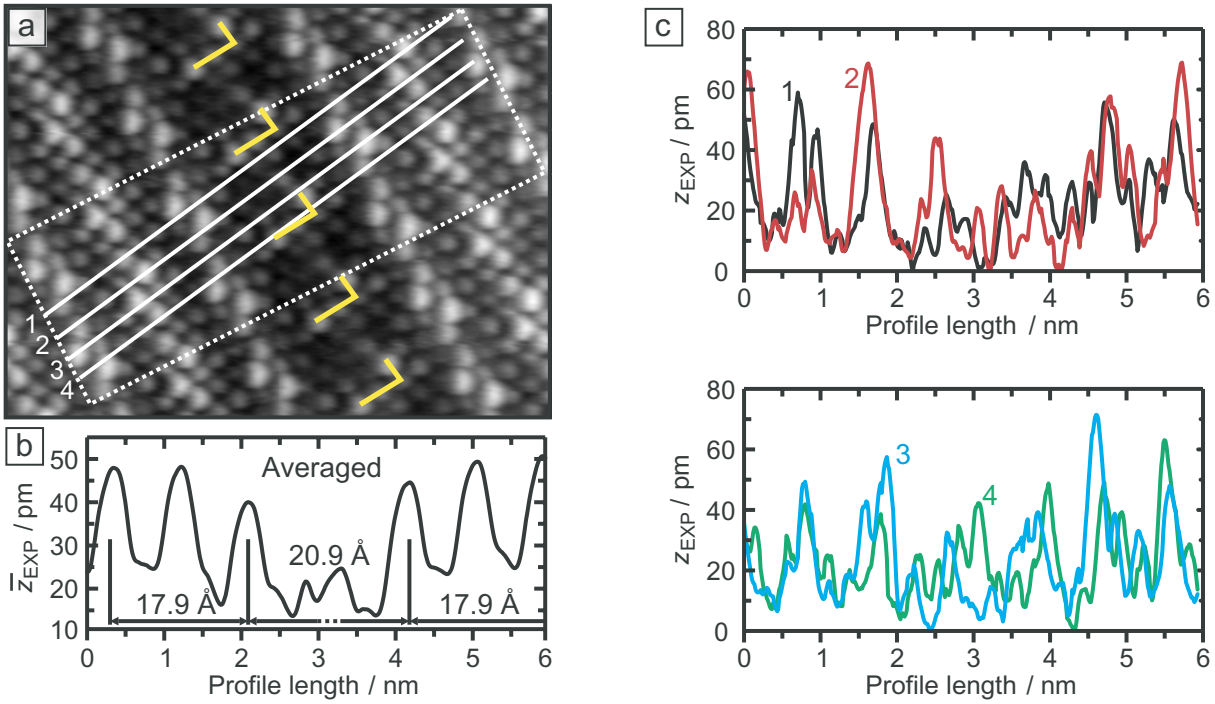

Figure 4. (a) Cutout from figure 3. Positions where line profiles have been taken across the type I boundary. (b) Averaged line profile taken within the rectangle (two unit cells in width) in the frame above. This emphasizes that such boundaries are reproduced as depressions within FM-DFM images. Averaging has been performed over 167 line profiles. (c) Single profiles along chains of O atoms across the APDB marked by white lines in the rectangle in subfigure (a). Such atom rows show heights different from average terrace height. Only the profile labelled 4 shows nearly no decrease in height over the APDB.

been taken along the white lines 1, 2, 3 and 4 in the image in figure 4(a). Between the linear oxygen rows, there exist sites with a mean height that is 10 pm lower than the average height of corresponding terrace sites (see figures 4(b)).

Already from the overview scan in figure 1 it becomes obvious that both types of APDBs exhibit sideways displacements from their initial line. For type I the displacements appear step-like and for type II as a change in gradient. For straight type I boundaries, the displacements seem to be preferred nucleation sites for palladium clusters [33] and may play that role as well for the zigzagged type II. Figures 5(a) and (d) show atomically resolved images of the sites of such lateral displacements within a type I APDB. Atomic positions, unit cells and structural elements are indicated again in parts (b), (d) and reproduced enlarged in the cutouts in (c), (f) of the figure together with the Burgers vector of the boundary. Geometric models of the surface have been built by adjusting the unit cell of the pristine film. There is excellent agreement between the imaged protrusions and the surface oxygen sublattice derived from the DFT model [21]. From this, it is deduced that the topmost oxygen layer is imaged also at the two dislocation jogs. This conclusion is supported, in particular, by the occurrence of important structural elements of that oxygen sublattice in the observed topography. Derived Burgers vectors ((3.1 ± 0.3) Å) are in agreement with earlier STM (3 Å) and SPA-LEED ((3.6 ± 0.3) Å)

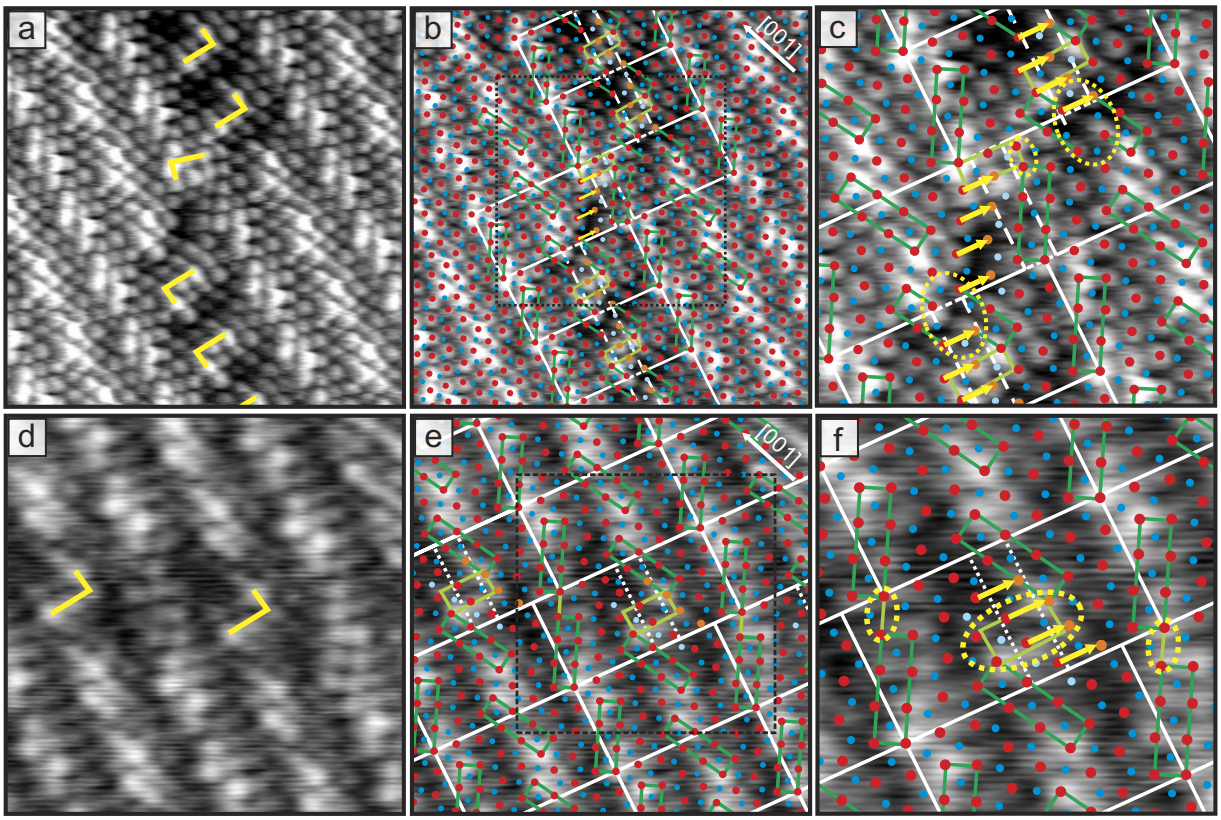

Figure 5. Atomic resolution FM-DFM image of two inequivalent points of sideways displacement (dislocation jogs) within a straight type I APDB in alumina/NiAl(110). (a) Image of a displacement along the short diagonal (along NiAl[$1\bar{1}0$]). (b) Geometrically adjusted model with inserted rows of four oxygen and aluminium sites at an angle of 60° to $\vec{b}_2$. (c) Enlarged cutout from (b). The lateral shift of the APDB axis equals a unit cell length. The large ellipses in (c) indicate the spacious oxygen arrangement along the boundary. The small ellipse describes a position where the ideal model of the domain structure is insufficient and predicts a closer arrangement than observed. Note the inversion symmetry in the topography of the structures marked with an yellow '*L*' at each side of the boundary. Scan area 6.1 nm × 6.1 nm. The cutout measures 3.5 nm × 3.5 nm. $\Delta f = -1.25$ Hz, $A_{\mathrm{OSC}} = 3.8$ Å, $V_S = -200$ mV. (d) Cascade of dislocation jogs off the initial axis along the oxide's long diagonal and towards the opposite direction. (e) Geometric model with inserted rows of four oxygen and aluminium sites at an angle of −60° to $\vec{b}_2$. (f) Enlarged cutout from (e). Reduced and enlarged square groups of O sites are encircled by dotted ellipses. Dotted ellipses highlight the sites of reduced and extended former squares of oxygen sites. Scan area 4.6 nm × 4.6 nm. The cutout measures 3 nm × 3 nm. $\Delta f = -5.2$ Hz, $A_{\mathrm{OSC}} = 3.8$ Å, $V_S = -200$ mV. Yellow arrows in (c) and (f) denote direction and length (3 Å) of the Burgers vector of the boundary.

results [15, 28]. To accommodate the unit cell model of the pristine film to the displacement point within the boundary in figure 5(a), the unit cell has been split parallel to the axis of the block of eight oxygen sites that is not affected in this boundary. An additional row of four oxygen atoms is inserted at an angle of 60° to $\vec{b}_2$. Note that these sites are inserted in a different fashion than into the blocks elsewhere along the APDB. The connecting square group on the respective crest is now extended into a group of six O sites as indicated by the light green rectangle in figures 5(b) and (c). The resulting model matches the observed sites and leaves the unit cell at the dislocation jog equivalent to those elsewhere along the APDB in terms of the number of sites and inserted sites. Added aluminium sites have been inferred geometrically and no computations are involved in the presented models. Large dotted loops in this case (figure 5(c)) encircle the positions with the spacious arrangement of the four oxygen atoms at the type I APDB, while the small dotted loop indicates a position where the adjusted model produces two sites in too close proximity. Here the simple extension of the unit cell along the b_2-direction does not match the observed sites as well as elsewhere in the image. The shift in the arrangement of structural elements at the dislocation jog seems to produce further slight distortions of the structure. Equivalent treatment of figure 5(d) produces the picture of an alternative dislocation jog which traverses the oxide unit cell along the second and longer diagonal. In fact a sequence of dislocation jogs is shown, which gives rise to further new atomic structures. Now four oxygen and four aluminium sites are inserted at an angle of −60° to $\vec{b}_2$ at each displacement point. The sideways displacement of the APDB I axis is again perpendicular to the initial line but now in the opposite direction. This in fact seems to be the prevalent case and dislocation jogs along the oxide's short diagonal like in figure 5(a) are seldom observed. As to be expected, it is now the square groups of oxygen sites on the other crest that are extended into rectangles with the typical 'L'-shaped topography at the dislocation jogs of figure 5(d). This becomes clear from the model in figure 5(e). Due to the sequence of dislocation jogs and the different orientation of the structural building blocks on neighbouring crests this reduces one type of square into a pair of oxygen sites while the other squares are again extended into a rectangular group of six oxygen sites. Both cases are highlighted by dotted ellipses in figure 5(f). As expected, the displacements within the straight domain boundaries represent two different variations of this type of boundary and not a zigzagged type II APDB. No component of the Burgers vector along the b_1 oxide lattice vector is observed. From available STM data as well as the FM-DFM results, it becomes clear that at its dislocation jogs the APDB I is always shifted by a whole oxide unit cell along b_2 or multiples of a unit cell in cascades of displacements. This is visible from the domain boundary in the middle of figure 1. Thus, one could consider them as arising from glide of one oxide half-plane along $\vec{b}_2$ by one unit cell length. In figure 5(a), the APDB I traverses the unit cell diagonally by one unit cell while figure 5(d) shows a cascade of displacements along the opposite diagonal. The preference for the long unit cell diagonal, which points away from the NiAl[1$\bar{1}$0] direction, for dislocation jogs will have its origin in the growth procedure. Oxide patches have been observed to nucleate at step edges [34]. Nucleation pins the step edge but changes in terrace shape towards the upper terrace may influence the size and shape of relaxing oxide domains and lead to dislocations in the oxide. Each direction of displacement is associated with one particular diagonal direction through the unit cell at the dislocation point.

At this point an interesting symmetry property of the dislocation jog in figure 5(a) becomes obvious. It is only present in the topography and has therefore been inaccessible to previous STM and SPA-LEED measurements. The characteristic bright protrusions in the middle of the

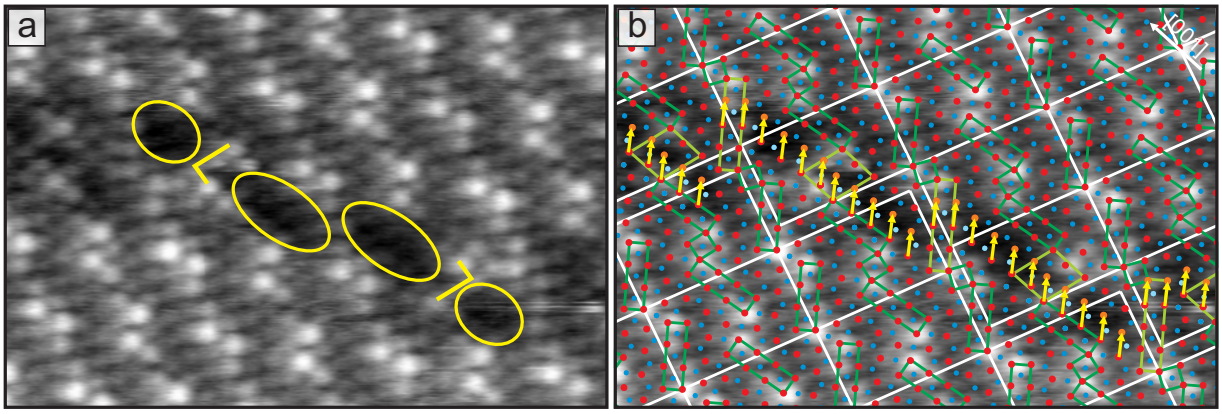

Figure 6. High-resolution FM-DFM image of a type II APDB in alumina/NiAl(110). Inequivalent types of subunits appear along this boundary. Two longer sections are centred at the structural elements marked by yellow angles while parts of a shorter type occur at the left and right edges of the image. The adjusted model is superimposed in (b). Yellow arrows denote direction and length (3 Å) of the Burgers vector of the boundary. Scan area 4.9 nm × 7.4 nm. $\Delta f = -2.66$ Hz, $A_{\mathrm{OSC}} = 3.8$ Å, $V_S = -100$ mV.

boundary appear differently on both sides of the displacement point. Despite their identical lateral structure the '*L*'-shaped groups seem rotated by 180° in their topography as indicated by the yellow angles in figure 5(a). These groups are recurring structural elements within the straight, but also the zigzagged APDB and their displacement jogs. The question arises, whether local atomic geometry or the interplay between interface and film integrity, and thus strain, dominates the surface structure. A further question, upon comparison with [22], is whether one interface arrangement could support different surface topographies.

3.3. Zigzagged (type II) antiphase domain boundaries

In this section, we present the first atomic resolution images of the surface oxygen arrangements on a zigzagged type II APDB. Figure 6(a) shows the drift corrected image. Yellow lines indicate topographically and symmetrically interesting structures. Figure 6(b) shows the same image with an additional model that we produced on the basis of the pristine unit cell structure. Displayed is a section of a type II APDB that is composed of linear segments traversing the unit cells along rows of the distorted hexagonal oxygen and aluminium lattices. These atom rows are at an angle of −60° to the b_2 vector of the oxide lattice and thus nearly parallel to NiAl[001]. In fact they are the same rows at which insertion occurs at the dislocation jog within the straight APDB I in figure 5(d). Linear segments differ in their length and are connected to one another by different kinds of step-like backlashes. The length seems to be prescribed by intersections with oxygen rows coming from the blocks of eight at an angle to $[1\bar{1}0]$, i.e. with the next axis of the quasihexagonal O sublattice. A backlash moves the beginning of the next linear segment upwards along the row of such a block in a way that it is extended into a block of ten oxygen sites. In this way, the block directly at the opposite end of the same unit cell can be extended, or the one in the next or second next unit cell down that crest. This corresponds to 7, 9 and 11

oxygen sites, i.e. six, eight and ten aluminium sites, in the linear segments. Details of all three types of structures are given in figures 7(a)–(g). For all three combinations of linear segments and backlashes, the APDB II follows a sawtooth like path but lines connecting equivalent points on neighbouring blocks of ten oxygen sites enclose different angles with $\vec{b}_2$. That is 0° in the case of seven atoms length, −30° for nine and −50° for 11 atoms in the linear segment. Relative to the long oxide diagonal this means +30°, 0° and −20°. In all three cases, the rectangular building block parallel to NiAl[001] is unaffected by the boundary while the connecting squares are split up and extended to compressed squares of nine sites with a clear depression in the middle.

The local arrangements are similar to those produced in the straight APDB as indicated by yellow 'L'-shaped lines. The two structural units of equal lateral appearance centred at the yellow 'L'-shapes in figure 6 exhibit the same planar symmetry relation already observed for the dislocation jog in figure 5(a). There seems to be a point inversion centre right between them. This is also reflected in the different depressions that further mark the boundary topographically. They have the shape of footprints pointing in opposite directions as highlighted by yellow loops. Emergence of these topographic structures is particularly interesting as these type II APDBs involve an additional direction of displacement in their Burgers vector along $\vec{b}_1$. It is surprising that structures which appear are almost identical to those observed in the case of APDB I. The additional component of the Burgers vector readily explains the appearance of the large distorted squares in figures 6 and 7 instead of blocks of six oxygen sites in figures 3–5. For figure 7(c) the surface aluminium sites have previously been determined by STM [28]. In that work eight Al_S positions have been found for the linear segment, which fits well to the nine O_S atoms in the FM-DFM image of that segment. This can be seen from the number and arrangement of inserted sites of light blue colour in figure 7(d). In this case the overall orientation towards $\vec{b}_2$ is an intermediate case at 0° to the long diagonal, which apparently dominates the global direction of most APDBs of the zigzagged type II. However, it is clear that this global path of an APDB II arises from sections of several nanometres length with different slope. Again, the APDBs appear as shallow depressions as in all of our FM-DFM images so far. Another group has observed them as depressions as well as protrusions [30]. Possible explanations as already proposed in that work could be the specific properties of the conducting silicon tips used but also electrostatic effects in that context. Our findings render protruding APDBs in FM-DFM images an impact of the tip. APDBs of type I have been reported to be oxygen deficient which is reflected in an electronic defect along the boundary [22]. Oxygen deficiency could be assumed for the zigzagged APDBs as well, which show similar electronic properties although not delocalized over large distance. Judged from our proposed models for the two topmost O_S and Al_S layers oxygen deficiency seems to be the case, but the interface oxygen and aluminium layers are not considered.

Observed Burgers vectors oriented with respect to substrate and oxide lattice geometric orientations are summarized for domain B in figure 7(h). With the oxide unit cell model in the background, global directions of the straight and zigzagged APDBs are indicated as bold solid lines. Local directions of the boundaries for example at the two kinds of dislocation jogs of the straight type I APDB are given as bold dashed lines. Also indicated are the average lattice directions for the distorted hexagonal surface aluminium (Al_S) and oxygen (O_S) layers. Two different Burgers vector directions at equal magnitude have been found for the two types of APDBs. They are inclined by ±24° off NiAl[1$\bar{1}$0] in the case of the straight type I and by ±35° for the zigzagged type II APDB in line with previous STM work. Global and local structure of the boundaries seem to be a compromise between the desired relaxation at the interface

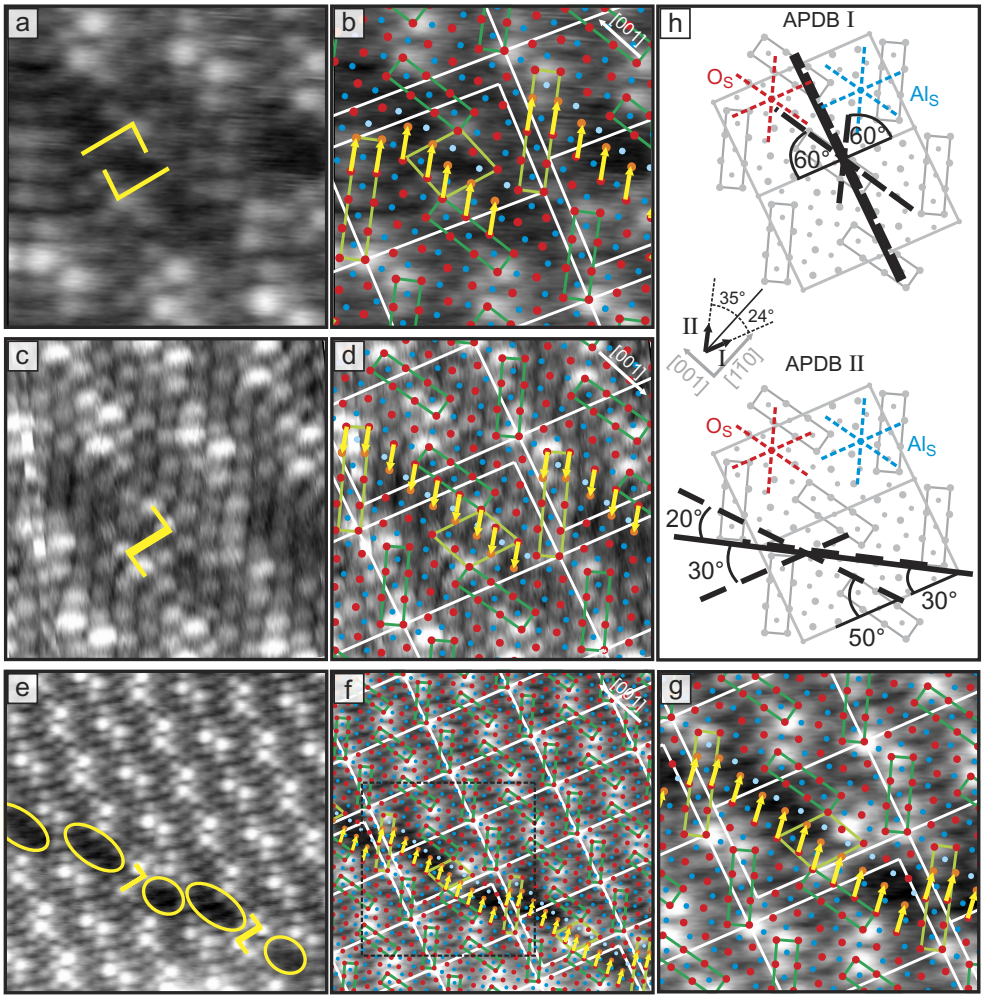

Figure 7. High-resolution FM-DFM images of subunits within the type II APDB in alumina/NiAl(110). Structures with 7, 9 and 11 oxygen sites in the linear segment are given in (a), (c) and (e). The adjusted models are superimposed in (b), (d), (f) and a cutout from (e) is shown in (g). Structural building blocks affected by the insertion of oxygen and aluminium rows (in lighter colour) are highlighted with light green lines. Yellow arrows denote the direction of the 3 Å long Burgers vector of the boundary. (a), (b) Scan area 3 nm × 3 nm, $\Delta f = -2.66$ Hz, $A_{\mathrm{OSC}} = 3.8$ Å, $V_S = -100$ mV. (c), (d) 3.4 nm × 3.4 nm, $\Delta f = -2$ Hz, $A_{\mathrm{OSC}} = 3.8$ Å, $V_S = -270$ mV. (e), (f) Scan area 6.5 nm × 6.5 nm, $\Delta f = -2.55$ Hz, $A_{\mathrm{OSC}} = 3.8$ Å, $V_S = -100$ mV. (g) Cutout from (f) 3.5 nm × 3.5 nm. In (c) and (d) the image is actually of an A domain and has been mirrored for comparability as no image of appropriate quality was available from this particular feature. Subfigure (h) summarizes the global (bold solid lines) and local (bold dashed lines) orientations of the straight type I and zigzagged type II APDB and their Burgers vectors with respect to substrate and oxide unit cell axes. Also given are the average orientations of rows in the quasihexagonal Al_S and O_S lattices (three intersecting blue and red dotted lines in each case).

with Burgers vectors along NiAl[1$\bar{1}$0] and advantageous paths through the unit cells along the quasihexagonal rows in the alumina film. This is corroborated by the reasonably small angle of the Burgers vectors to NiAl[1$\bar{1}$0], their direction along quasihexagonal O_S rows and the absence of a third direction for APDBs with a Burgers vector along the third quasihexagonal axis. In the latter case, the relaxation would be almost along the incommensurate direction and perpendicular to the direction of most efficient strain relief. Consequently it is not observed. These observations are also satisfied by straight APDBs and their frequent step dislocations. These dislocation jogs also satisfy the rule that film rupture follows particular paths through the oxide unit cell but their direction is not preferentially along the direction closest to the commensurate NiAl[1$\bar{1}$0] direction. Therefore, it can be assumed that dislocation jogs are induced by growth effects on a larger length scale.

The high-resolution images presented give insight into the topography of the alumina on NiAl(110) and reveal further subtle details of the atomic arrangements, especially of structural elements. It is interesting to note that the most prominent structural elements, the two differently oriented blocks of eight oxygen sites, differ not only in their height span, but also in their length. The fact that the expected glide-mirror symmetry has not been observed is interpreted as being a result of the influence from the film substrate interface. Obviously, the film structure is not entirely two dimensional. This difference in length reflects the underlying substrate influence that causes one type of these structural elements, namely the one nearly parallel to the NiAl[001] direction to be involved in the type I APDB. The contrary has not been observed so far. This may also explain why domain widths and sideways displacements of the APDBs are always given by multiples of a whole unit cell length. For the oxide surface this translates locally into a particular path that APDBs take through the unit cell. Interestingly, this is the case despite the variety of different sites in its structure. From figure 7 it can be seen that this holds for APDBs of type II as well. They also show a regular structure with lateral displacements realized at the same structural building blocks that are affected in the straight APDBs. Consequentlly, both types of APDBs then produce a symmetry aspect which is only present in the topography: an inversion symmetry between different structural building blocks with characteristic height along the respective boundary.

Results presented above connect nicely to ultrathin alumina films on $Ni_3Al(111)$ and on Cu–9%Al(111) [35, 36], which may be considered to be members of a new class of two-dimensional alumina phases. They are grown by selective oxidation of the aluminium of different transition metal aluminium alloys. Interestingly, these surface oxides show structural buildings blocks or surface layers that are similar or even identical to those of the alumina on NiAl(110) studied in this work. For example, the ultrathin alumina overlayer on the Cu–9%Al(111) surface produces a phase that strongly resembles in orientation, shape and size of the unit cell the alumina on NiAl(110). The unit cells of surface oxygen and interface aluminium layers of both films are of identical structure including the existence of the characteristic blocks of eight O sites which are connected into rows by square arrangements of oxygen atoms. Only the antiphase domain boundaries are missing in the alumina on Cu–9%Al(111) case. At this point, several conclusions can be drawn. The topography of the surface oxygen layer is not directly determined by the interface in a geometrical sense by bond length or inserted atoms. This is also supported by the regular appearance in STM images showing the oxide's surface and the topography in the presented FM-DFM images. In contrast to what one might expect from the incommensurability along the NiAl[001] direction, images show no random changes in their topopgraphy. Also one could expect surface oxygen sites to

be lifted upwards by interface aluminium atoms other than just in the blocks of eight O atoms. As the same surface structure appears above different interfaces, i.e. on Cu–9%Al(111) and on NiAl(110), the crests and troughs and thus the typical structural elements could be governed by the epitaxial relation in an indirect fashion. For alumina/NiAl(110) the oxide cells could compensate the row matching by a buckling of their oxygen surface which would be in line with the reduced O–O distances in the structural elements and the sinosoidal deviation of the Al_S and O_S layers from a regular hexagonal lattice.

The large variety in the topography of this alumina surface, especially at the APDBs, suggests that a significant number of adsorption sites can be expected for one species. Particularly interesting is the question regarding the symmetry of adsorption sites with equal lateral structure, on the domain and on APDBs. However, to fully determine their whereabouts one would have to study the complete force field above the surface to determine minima of the potential energy surface. In any case, the obtained surface sensitivity with topographic contrast at high spatial resolution is a good starting point. It is anticipated that the presented results stimulate further theoretical treatment of the APDBs.

4. Summary

In conclusion, atomically resolved FM-DFM images have been obtained from the ultrathin alumina film grown on NiAl(110). Images allow the clear determination of the atomic structure of the surface oxygen layer and adjustment of the existing model for the unit cell of the pristine film to newly resolved features in the APDBs. This is shown in detail for the straight APDB (type I) and for the first time also for two types of dislocation jogs in type I APDBs and three inequivalent structural units of the zigzagged APDB (type II). Such high-resolution images exhibit a characteristic contrast, which allows a fairly straightforward recognition and assignment of the structure and discrimination between surface species. Images with this contrast show the surface oxygen sublattice as protrusions and match calculated data even with respect to topographic height indicating the extremely high surface sensitivity of the technique. This virtue of forces as a measurable quantity is somewhat complementary to the insight gained by current measurements. In particular it has been possible to observe a point inversion between structures within individual APDBs of both types, which is only present in topography. Furthermore, the impact of tip material and local electronic properties has been marginal in the performed experiments and the APDBs could eventually be shown to be actual depressions. It has been possible to quantify subtle differences among structural elements and relate them to the growth behaviour of straight APDBs together with recurring structures in different types of boundaries. Interesting for further studies is an emerging class of ultrathin alumina films with similar surface structure building blocks, while growing on different substrates. The atomic resolution of our stable low-temperature force microscope, in combination with the before mentioned topographic contrast, enables thorough analysis of such surfaces.

Acknowledgments

We wish to thank G Thielsch who helped to keep the machine running and thus the spirit of the work group high. Also, we thank N R Scott for proofreading our manuscript.

References

[1] Simon G H, König T, Kulawik M, Rust H-P, Heyde M and Freund H-J 2008 *Phys. Rev.* B **78** 113401
[2] Bragg L and Nye J F 1947 *Proc. R. Soc.* A **190** 474
[3] Bassett G A, Menter J W and Pashley D W 1958 *Proc. R. Soc.* A **246** 345
[4] Jacobs M H, Pashley D W and Stowell M J 1966 *Phil. Mag.* **13** 129
[5] Birgeneau R J and Horn P M 1986 *Science* **232** 329
[6] Barth J V, Brune H, Ertl G and Behm R J 1990 *Phys. Rev.* B **42** 9307
[7] Feenstra R M, Slavin A J, Held G A and Lutz M A 1991 *Phys. Rev. Lett.* **66** 3257
[8] Schuster R, Ertl G and Behm R J 1992 *Phys. Rev. Lett.* **69** 2547
[9] Henzler M 1984 *Appl. Phys.* A **34** 205
[10] Fukui K and Iwasawa Y 2000 *Surf. Sci.* **464** L719
[11] Kubo T and Nozoye H 2001 *Phys. Rev. Lett.* **86** 1801
[12] Yi I, Nishi R, Sugimoto Y and Morita S 2007 *Appl. Surf. Sci.* **253** 3072
[13] Jensen M C R, Venkataramani K, Helveg S, Clausen B S, Reichling M, Besenbacher F and Lauitsen J V 2008 *J. Phys. Chem.* C **112** 16953
[14] Barth C and Henry C R 2009 *New J. Phys.* **11** 043003
[15] Libuda J, Winkelmann F, Bäumer M, Freund H-J, Bertrams Th, Neddermeyer H and Müller K 1994 *Surf. Sci.* **318** 61
[16] Bäumer M and Freund H-J 1999 *Prog. Surf. Sci.* **61** 127
[17] Ceballos G, Song Z, Pascual J I, Rust H-P, Conrad H, Bäumer M and Freund H-J 2002 *Chem. Phys. Lett.* **359** 41
[18] Kulawik M, Nilius N and Freund H-J 2006 *Phys. Rev. Lett.* **96** 036103
[19] Schintke S and Schneider W-D 2004 *J. Phys.: Condens Matter* **16** R49
[20] Schnadt J, Michaelides A, Knudsen J, Vang R T, Reuter K, Laesgaard E, Scheffler M and Besenbacher F 2006 *Phys. Rev. Lett.* **96** 146101
[21] Kresse G, Schmid M, Napetschnig E, Shishkin M, Köhler L and Varga P 2005 *Science* **308** 1440
[22] Schmid M, Shishkin M, Kresse G, Napetschnig E, Varga P, Kulawik M, Nilius N, Rust H-P and Freund H-J 2006 *Phys. Rev. Lett.* **97** 046101
[23] Rust H-P, Heyde M and Freund H-J 2006 *Rev. Sci. Instrum* **77** 043710
[24] Heyde M, Sterrer M, Rust H-R and Freund H-J 2005 *Appl. Phys. Lett.* **87** 083104
[25] Heyde M, Simon G H, Rust H-P and Freund H-J 2006 *Appl. Phys. Lett.* **89** 263107
[26] Horcas I, Fernández R, Gómez-Rodríguez J M and Colchero J 2007 *Rev. Sci. Instrum.* **78** 013705
[27] Jaeger R M, Kuhlenbeck H, Freund H-J, Wuttig M, Hoffmann W, Franchy R and Ibach H 1991 *Surf. Sci.* **259** 235
[28] Kulawik M, Nilius N, Rust H-P and Freund H-J 2003 *Phys. Rev. Lett.* **91** 256101
[29] McCarty K F, Pierce J P and Carter B 2006 *Appl. Phys. Lett.* **88** 141902
[30] Pang C L, Raza H, Haycock S A and Thornton G 2002 *Phys. Rev.* B **65** 201401
[31] Schwarz A, Allers W, Schwarz U D and Wiesendanger R 2000 *Phys. Rev.* B **61** 2837
[32] Hofer W A, Foster A S and Shluger A L 2003 *Rev. Mod. Phys.* **75** 1287
[33] Napetschnig E, Schmid M and Varga P 2007 *Surf. Sci.* **601** 3233
[34] Ulrich S, Nilius N and Freund H-J 2007 *Surf. Sci.* **601** 4603
[35] Schmid M, Kresse G, Buchsbaum A, Napetschnig E, Gritschneder S, Reichling M and Varga P 2007 *Phys. Rev. Lett.* **99** 196104
[36] Napetschnig E, Schmid M and Varga P 2008 *Surf. Sci.* **602** 1750